



Hydrogen production by steam reforming of simulated liquefied natural gas (LNG) over nickel catalyst supported on mesoporous phosphorus-modified alumina xerogel

Yongju Bang^a, Seung Ju Han^a, Jaekyeong Yoo^a, Jung Ho Choi^a, Jong Kwon Lee^a,
Ji Hwan Song^a, Jinwon Lee^{b,1}, In Kyu Song^{a,*}

^a School of Chemical and Biological Engineering, Institute of Chemical Processes, Seoul National University, Shinlim-dong, Kwanak-ku, Seoul 151-744, South Korea

^b Department of Chemical and Biomolecular Engineering, Sogang University, Seoul 121-742, South Korea

ARTICLE INFO

Article history:

Received 26 July 2013

Received in revised form 22 October 2013

Accepted 9 November 2013

Available online 18 November 2013

Keywords:

Hydrogen production

Steam reforming of LNG

Mesoporous phosphorus-modified alumina

Nickel catalyst

Epoxide-driven sol–gel method

ABSTRACT

A series of nickel catalysts supported on mesoporous phosphorus-modified alumina xerogel (Ni/XPA, X = P/Al molar ratio) were prepared by an epoxide-driven sol–gel method and a subsequent incipient impregnation method, and they were applied to the hydrogen production by steam reforming of simulated liquefied natural gas (LNG). All the calcined phosphorus-modified alumina xerogel supports (XPA, X = P/Al molar ratio) retained a mesoporous structure with amorphous crystalline phase. The amount of penta-coordinated aluminum species increased with increasing X (P/Al molar ratio) of XPA supports. Although the calcined Ni/XPA catalysts retained both nickel oxide phase and nickel aluminate phase, relative distribution of nickel species of the catalysts was different depending on X (P/Al molar ratio). Among the catalysts, Ni/0.05PA catalyst showed the highest binding energy of nickel species. Crystallite size of metallic nickel increased with increasing X (P/Al molar ratio) in the reduced Ni/XPA catalysts. However, Ni/0.05PA catalyst showed the largest amount of strong hydrogen-binding sites and exhibited the largest amount of adsorbed methane in the H₂-TPD and CH₄-TPD measurements, respectively. Catalytic performance in the steam reforming of LNG over Ni/XPA catalysts showed a volcano-shaped trend with respect to X (P/Al molar ratio). This result was well correlated with the amount of adsorbed methane calculated from CH₄-TPD measurements. Among the catalysts tested, Ni/0.05PA catalyst with the highest affinity toward methane showed the best catalytic performance in hydrogen production by steam reforming of LNG.

© 2013 Elsevier B.V. All rights reserved.

1. Introduction

Various researches for utilizing new renewable energy have been widely conducted around the world [1–3]. This trend is accelerated with increasing concerns about environmental issues such as global warming, air pollution, water pollution, acid rain, and ozone layer depletion. One way to overcome these environmental problems is to develop a new energy supply system using energy source with low carbon content. In this respect, hydrogen has attracted much attention as the most promising energy carrier due to its carbon-free nature. Furthermore, it is favorable to use hydrogen rather than fossil fuels in many ways because hydrogen is clean and does not emit any pollutants such as NO_x

and SO_x during the combustion [4]. High energy density of hydrogen (>120 kJ/g) is another advantage of hydrogen utilization [5]. These characteristics of hydrogen lead to a development of several hydrogen-related products such as hydrogen vehicle, fuel processor, combustion engine, and residential fuel cell [6,7].

Catalytic steam reforming of methane has been widely employed as an efficient process for hydrogen production, although high reaction temperature (>800 °C) is required for steam reforming of methane due to its endothermic nature ($\Delta H^{\circ}_{298\text{ K}} = +206\text{ kJ/mol}$) [8,9]. Liquefied natural gas (LNG), which is mainly composed of methane, has been accepted as a promising source for hydrogen production by steam reforming due to its abundance and its availability derived from well-established infrastructure in the modern cities [10,11].

Nickel-based catalysts are known to be highly active in the steam reforming reaction. However, they are vulnerable to catalyst deactivation due to carbon deposition and nickel sintering during the reaction [12–15]. For this reason, various metal oxides

* Corresponding author. Tel.: +82 2 880 9227; fax: +82 2 889 7415.

E-mail addresses: jinwonlee@sogang.ac.kr (J. Lee), inksong@snu.ac.kr (I.K. Song).

¹ Tel.: +82 2 705 8919; fax: +82 2 711 0439.

and metals have been investigated as supports and promoters to resolve deactivation problem and to enhance catalytic activity of nickel-based catalysts. For example, mesoporous alumina xerogel has been employed as a support for nickel catalyst in order to mitigate mass transfer limitation of reactants and to enhance nickel dispersion of the catalyst [16]. Ceria support is also used for long-term stability of nickel catalyst in the steam reforming of methane due to its excellent redox property [17]. Furthermore, it has been reported that Ni–Mg–O catalyst shows higher activity and stability in the steam reforming of methane than a commercial reforming catalyst under reaction condition of low steam to carbon ratio [18]. Synergistic effect of Mg and Cu addition into nickel catalyst was also investigated [19].

However, only a few researches have focused on promotion of nickel-based catalysts via addition of non-metal elements such as boron, sulfur, and phosphorus [20–22]. Non-metal elements are useful for alleviation of carbon deposition on the surface of nickel-based catalyst in the steam reforming reaction, because these non-metal elements predominantly retain rich valence electrons and high electronegativity compared to metal elements. Moreover, this feature of non-metal elements may cause changes in textural and surface properties of nickel-based catalyst by forming a defective and asymmetrical electronic structure. It is expected that nickel dispersion, crystalline structure, and chemical affinity with reactant molecule of nickel-based catalyst can be modified by the addition of non-metal element. In particular, addition of phosphorus into alumina is known to be effective for stabilization of framework and modification of Lewis acid property of alumina [23]. Therefore, a systematic investigation on the effect of phosphorus addition on the catalytic activity and physicochemical property of nickel–alumina catalyst would be worthwhile.

In this work, a series of nickel catalysts supported on mesoporous phosphorus-modified alumina xerogel were prepared by an epoxide-driven sol–gel method and a subsequent incipient wetness impregnation method. The prepared nickel catalysts were applied to the hydrogen production by steam reforming of simulated LNG. The effect of phosphorus addition on the physicochemical properties and catalytic activities of the catalysts in the steam reforming of LNG was investigated. The catalysts were characterized by N₂ adsorption–desorption, XRD, TPR, XPS, UV–vis-DRS, TEM, H₂-TPD, and CH₄-TPD to elucidate their catalytic performance.

2. Experimental

2.1. Preparation of nickel catalyst supported on mesoporous phosphorus-modified alumina xerogel

A series of mesoporous phosphorus-modified alumina xerogel supports were prepared by an epoxide-driven sol–gel method [24–26]. 16.1 g of aluminum precursor (aluminum nitrate nonahydrate, Sigma-Aldrich) was dissolved in anhydrous ethanol (100 ml) at room temperature with vigorous stirring for 30 min (Solution A). For sufficient hydration of aluminum species, a small amount of distilled water (2.3 ml) was added into the Solution A (Solution B). Phosphoric acid (Sigma-Aldrich), which served as a structural modifier, was then introduced into the solution B (Solution C). During this process, P/Al molar ratio was adjusted to be 0, 0.02, 0.05, 0.10, and 0.20. After stirring the Solution C for 20 min, propylene oxide as a gelation agent was added into the Solution C to induce polycondensation between metal species. White opaque gel was obtained within 20 min after the addition of propylene oxide. The gel was aged for 2 days and it was dried in a convection oven for 2 days at 80 °C. The resulting powder was calcined at 700 °C for 5 h to yield a mesoporous phosphorus-modified alumina xerogel support. The prepared mesoporous phosphorus-modified

alumina xerogel supports were denoted as XPA (X=0, 0.02, 0.05, 0.10, and 0.20), where X represented the P/Al molar ratio.

A set of nickel catalysts supported on mesoporous phosphorus-modified alumina xerogel supports (XPA) were prepared by an incipient wetness impregnation method. Nickel precursor (nickel nitrate hexahydrate, Sigma-Aldrich) was dissolved in anhydrous ethanol for 20 min. The nickel precursor solution was added dropwise to XPA support for impregnation. The supported nickel catalyst was dried at 80 °C overnight in a convection oven. As-prepared catalyst sample was finally calcined at 700 °C for 5 h to yield a nickel catalyst supported on mesoporous phosphorus-modified alumina xerogel. The prepared nickel catalysts were denoted as Ni/XPA (X=0, 0.02, 0.05, 0.10, and 0.20). The Ni loading was fixed at 20 wt% in all the Ni/XPA catalysts.

2.2. Characterization

Nitrogen adsorption–desorption measurements were conducted to examine textural properties of XPA (X=0, 0.02, 0.05, 0.10, and 0.20) supports and Ni/XPA (X=0, 0.02, 0.05, 0.10, and 0.20) catalysts using a BELSORP-mini II (BEL Japan) apparatus. All the supports and catalysts were degassed at 150 °C for 6 h by rotary vacuum pump for removal of moisture and other adsorbed gases on the surface of samples. Nitrogen adsorption–desorption isotherms were obtained at –196 °C (liquid nitrogen temperature). Surface areas were calculated by the Brunauer–Emmett–Teller (BET) method. ICP-AES (ICPS-1000IV, Shimadzu) analyses were carried out in order to verify compositions of the supports and catalysts. X-ray diffraction (XRD) patterns of the supports and catalysts were obtained with a D-Max2500-PC (Rigaku) diffractometer operated at 50 kV and 150 mA. Data collection was performed with a scan rate of 5 °C/min using Cu K α radiation (λ = 1.541 Å). For the XRD of reduced Ni/XPA catalysts, 0.1 g of each calcined Ni/XPA catalyst was reduced with a mixed stream of H₂ (3 ml/min) and N₂ (30 ml/min) at 700 °C for 3 h. Chemical states of aluminum and phosphorus species in the XPA supports were examined by ²⁷Al MAS NMR (magic angle spinning nuclear magnetic resonance) and ³¹P MAS NMR spectra obtained using a AVANCE 400 WB spectrometer operated at resonance frequencies of 104 MHz for ²⁷Al and 162 MHz for ³¹P. MAS frequencies were kept at 10 kHz for ²⁷Al MAS NMR and 7 kHz for ³¹P MAS NMR. Temperature-programmed reduction (TPR) measurements were conducted in order to examine metal-support interaction between nickel species and XPA support. 50 mg of each catalyst was charged into the U-shaped quartz reactor and then it was reduced with a mixed stream of H₂ (2 ml/min) and N₂ (20 ml/min). TPR profiles were collected using a thermal conductivity detector (TCD) at a heating rate of 5 °C/min from room temperature to 1000 °C. X-ray photoelectron spectroscopy (XPS) analyses were conducted to determine binding energies of nickel species in the calcined Ni/XPA catalysts using a AXIS-HSi (KRATOS) apparatus. All the spectra were calibrated taking C 1s peak at 284.5 eV as a reference. UV–vis-diffuse reflectance (UV–vis-DRS) spectra of the calcined Ni/XPA catalysts were obtained using a Lambda-35 (Perkin-Elmer) spectrometer within the range of 400–800 nm to examine coordination state of nickel species. To examine morphological features of the reduced catalysts, TEM analyses (JEM-2100, Jeol) were carried out. Ex-situ reduction with a mixed stream of H₂ (3 ml/min) and N₂ (30 ml/min) was preliminarily conducted before TEM analyses of the reduced catalysts. H₂ temperature-programmed desorption (H₂-TPD) measurements were conducted to measure the amount of hydrogen uptake and hydrogen-binding strength on the surface of reduced Ni/XPA catalysts using a BELCAT-B (BEL Japan) apparatus equipped with a thermal conductivity detector (TCD). 50 mg of each catalyst was introduced in a quartz cell and it was reduced at 700 °C for 3 h with 5% H₂/Ar flow (50 ml/min), and subsequently, it was

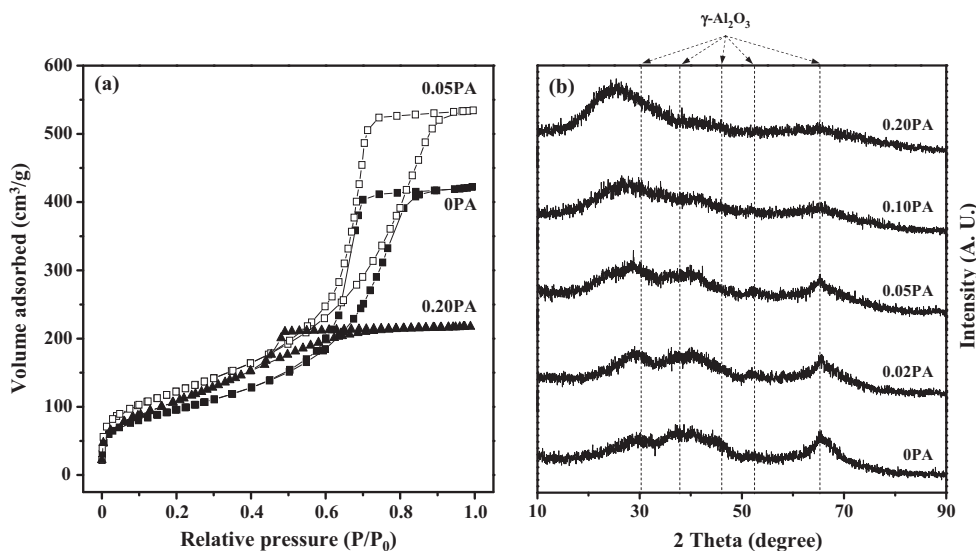


Fig. 1. (a) Nitrogen adsorption–desorption isotherms of calcined XPA ($X=0, 0.05$, and 0.20) supports, and (b) XRD patterns of calcined XPA ($X=0, 0.02, 0.05, 0.10$, and 0.20) supports.

purged with Ar flow (50 ml/min) for 10 min at 700 °C. After cooling the cell to 50 °C under Ar flow (50 ml/min), 5% H₂/Ar flow (50 ml/min) was introduced to saturate the catalyst surface with hydrogen for 30 min. To remove physisorbed hydrogen on the surface of the catalyst, temperature of the cell was maintained at 100 °C for 1 h. After the cell was cooled to 50 °C, H₂-TPD measurement was conducted within the temperature range of 50–950 °C under Ar flow (50 ml/min). In order to elucidate adsorption behavior of methane on the reduced catalysts, CH₄ temperature-programmed desorption (CH₄-TPD) measurements were carried out in a conventional flow system. 0.1 g of each catalyst was loaded into the U-shaped quartz reactor. It was reduced at 700 °C for 3 h with a mixed stream of H₂ (3 ml/min) and He (30 ml/min). The reactor was then cooled to room temperature under He flow (30 ml/min) and it was purged for 20 min using He flow (30 ml/min). 20 ml of methane was then pulsed into the reactor every minute at room temperature under a flow of helium (5 ml/min), until the surface of the catalyst was saturated with methane. After purging the reactor with He flow (30 ml/min) at 50 °C for 1 h to remove physisorbed methane, temperature of the reactor was increased from room temperature to 900 °C at a heating rate of 10 °C/min under a flow of helium (10 ml/min). H₂ flow (2 ml/min) was also introduced to the reactor during the measurement for complete desorption of adsorbed carbon species. Desorbed species were detected using a GC–MSD (6890N GC-5975MSD, Agilent). The amount of carbon deposition on the used catalysts after the reaction was determined by CHNS elemental analyses (CHNS 932, Leco).

2.3. Catalytic test in the steam reforming of LNG

Catalytic performance of Ni/XPA ($X=0, 0.02, 0.05, 0.10$, and 0.20) catalysts in the steam reforming of LNG was evaluated in a fixed-bed quartz reactor. LNG used in this work was simulated LNG composed of methane (92.0 vol%) and ethane (8.0 vol%). 0.1 g of each catalyst was loaded into the reactor, and it was preliminarily reduced with a mixed stream of H₂ (3 ml/min) and N₂ (30 ml/min) at 700 °C for 3 h. Steam reforming of LNG was conducted at 600 °C for 1000 min. Feed composition was fixed at CH₄ (4.6 ml/min), C₂H₆ (0.4 ml/min), H₂O (11.3 ml/min), and N₂ (30 ml/min). Steam to carbon molar ratio was kept at 2.09. It was preliminarily confirmed that mass transfer limitation was negligible at the total feed flow rate of 27,790 ml/h/g-catalyst. Reaction products were

periodically analyzed with an on-line gas chromatograph (ACME 6000, Younglin) equipped with a thermal conductivity detector (TCD). LNG conversion and hydrogen yield over Ni/XPA catalysts were calculated by the following equations. All the flow rates of fluids were in standard ambient temperature and pressure (SATP; 25 °C, 1 atm).

$$\text{LNG conversion(\%)} = \left(1 - \frac{F_{\text{CH}_4, \text{out}} + F_{\text{C}_2\text{H}_6, \text{out}}}{F_{\text{CH}_4, \text{in}} + F_{\text{C}_2\text{H}_6, \text{in}}}\right) \times 100 \quad (1)$$

$$\text{Hydrogen yield(\%)} = \frac{F_{\text{H}_2, \text{out}}}{2 \times F_{\text{CH}_4, \text{in}} + 3 \times F_{\text{C}_2\text{H}_6, \text{in}}} \times 100 \quad (2)$$

3. Results and discussion

3.1. Characterization of calcined supports

Nitrogen adsorption–desorption measurements were conducted to examine textural properties of XPA ($X=0, 0.02, 0.05, 0.10$, and 0.20) supports calcined at 700 °C for 5 h. Fig. 1(a) shows the nitrogen adsorption–desorption isotherms of 0PA, 0.02PA, and 0.20PA supports. All the XPA supports exhibited IV-type isotherms, which were attributed to the well-developed mesoporous structure [27]. H₂-type hysteresis loops were also observed in the isotherms of XPA supports, indicating the existence of mesopores with narrow necks and wide bodies in the XPA supports [27]. It is interesting to note that the positions of limiting nitrogen uptake region were changed with a variation of P/Al molar ratio. 0PA and 0.05PA supports retained similar shapes of hysteresis loops, except that 0.05PA support showed higher height of limiting nitrogen uptake than 0PA support. On the other hand, 0.20PA support exhibited a quite different hysteresis loop with relatively small area and low steepness. A close examination revealed that the amount of limiting nitrogen uptake was maintained until low relative pressure at ca. 0.45–0.50 in the desorption branch of 0.20PA support. These results imply that 0.20PA support retained a mesoporous structure with low uniformity and small pore size compared to 0PA and 0.05PA supports [28]. Thus, the mesoporous structure of phosphorus-modified alumina xerogel support could be modified by changing P/Al molar ratio.

Detailed textural properties of calcined XPA ($X=0, 0.02, 0.05, 0.10$, and 0.20) supports are summarized in Table 1. Actual P/Al

Table 1
Textural properties of supports (XPA) and catalysts (Ni/XPA) calcined at 700 °C for 5 h.

Sample		Ni/(P + Al) molar ratio ^a	P/Al molar ratio ^a	Surface area (m ² /g) ^b	Pore volume (cm ³ /g) ^c	Pore diameter (nm) ^d
Support	OPA	–	0	345	0.65	7.6
	0.02PA	–	0.02	414	0.91	8.8
	0.05PA	–	0.05	444	0.83	7.4
	0.10PA	–	0.10	395	0.36	3.7
	0.20PA	–	0.20	388	0.34	3.3
Catalyst	Ni/OPA	0.18	0	230	0.46	7.9
	Ni/0.02PA	0.18	0.02	271	0.64	9.4
	Ni/0.05PA	0.18	0.05	274	0.55	8.0
	Ni/0.10PA	0.18	0.10	280	0.26	3.7
	Ni/0.20PA	0.18	0.20	282	0.21	3.0

^a Determined by ICP-AES measurement.

^b Calculated by the BET equation.

^c Total pore volume at $P/P_0 \sim 0.995$.

^d Mean pore diameter.

molar ratios in the XPA supports were well matched with the designed values. All the XPA supports exhibited large surface area ($>340 \text{ m}^2/\text{g}$), large pore volume ($>0.3 \text{ cm}^3/\text{g}$), and large pore diameter ($>3 \text{ nm}$), indicating successful formation of mesoporous structure in spite of high temperature calcination process (700 °C for 5 h) during the preparation of supports. It is noteworthy that surface area of XPA ($X=0.02, 0.05, 0.10$, and 0.20) supports was larger than that of OPA support, and surface area of XPA supports showed a volcano-shaped trend. This was because phosphate groups dispersed in the framework of phosphorus–aluminum gel modified the surface and pore structure of aluminum oxide. In other words, addition of phosphorus into alumina matrix was responsible for generation of complex surface morphology and porous structure of alumina. Excessive addition of phosphorus was revealed to be disadvantageous due to hindrance of phosphate or phosphorus-containing oxide on the formation of mesoporous network in alumina. In the similar manner, pore volume and pore diameter of XPA supports also showed volcano-shaped trends.

Crystalline structures of calcined XPA ($X=0, 0.02, 0.05, 0.10$, and 0.20) supports were examined by XRD measurements as shown in Fig. 1(b). Diffraction peaks corresponding to $\gamma\text{-Al}_2\text{O}_3$ phase were detected in all the XPA supports. However, intensities for diffraction peaks decreased with increasing P/Al molar ratio in the XPA supports. This means that the addition of phosphorus makes alumina support more amorphous by acting as a structural modifier. In addition, phosphorus might induce a defective structure in alumina support during the calcination process. No distinct phosphorus-related species such as aluminum phosphate were observed in the XRD patterns of XPA supports, representing that phosphorus species were amorphously distributed in alumina. Only a broad diffraction band at $2\theta = 25^\circ$ attributed to incorporation of phosphorus into alumina lattice was detected in the 0.20PA support.

In order to elucidate chemical states of aluminum species in the calcined XPA ($X=0, 0.02, 0.05, 0.10$, and 0.20) supports, ^{27}Al MAS NMR spectra of the supports were obtained as shown in Fig. 2. According to the previous studies [29,30], there are three types of aluminum species in transition alumina; octa-coordinated aluminum (Al^{VI}), penta-coordinated aluminum (Al^{V}), and tetra-coordinated aluminum (Al^{IV}). Cross-linking between octa-coordinated aluminum species of aluminum hydroxide is known to cause migration or transformation of aluminum into penta- and tetra-coordinated aluminum species [31]. A defective and vacant structure in alumina formed in this process is related to the generation of penta-coordinated aluminum species. As presented in Fig. 2, all the calcined XPA supports retained three peaks at around 0, 30, and 60 ppm, corresponding to octa-coordinated aluminum, penta-coordinated aluminum, and tetra-coordinated aluminum, respectively. Relative distribution of each aluminum

species was calculated from the deconvoluted peaks of NMR spectra as listed in Table 2. It is noteworthy that the amount of octa-coordinated aluminum decreased while that of penta- and tetra-coordinated aluminum increased with increasing P/Al molar ratio of the XPA supports. This indicates that phosphorus caused transition of octa-coordinated aluminum species in the XPA supports into coordinately unsaturated penta- and tetra-coordinated aluminum species through the formation of Al–O–P linkage in composite oxide as reported in the literature [32]. This might be because rapid gelation by phosphorus species located in the XPA supports with higher P/Al molar ratio induced more defective and vacant sites, resulting in much coordinately unsaturated aluminum species. Penta-coordinated aluminum is known to act as a Lewis acid site which can serve as an anchoring site for metal ions [33]. Therefore, it is expected that nickel species located on the surface of XPA support with high population of penta-coordinated aluminum more abundantly interact with the support than those on the XPA support with low population of penta-coordinated aluminum. Nevertheless, chemical shift of penta-coordinated aluminum species in the XPA supports moved to a lower chemical shift with increasing P/Al molar ratio, demonstrating that strength of aluminum species for anchoring nickel species decreased with increasing P/Al molar ratio. The explanation for this phenomenon is that the addition of electron-rich phosphorus was effective for changing aluminum to be less electron deficient (more shielded).

^{31}P MAS NMR spectra of calcined XPA ($X=0.02, 0.05, 0.10$, and 0.20) supports are presented in Fig. 3. All the XPA supports exhibited a broad signal within the chemical shift ranging from 0 to -30 ppm . This broad band is related to the small amount of phosphorus species and various environments around phosphorus species. It was found that NMR peak moved to a lower chemical shift (upfield) region with increasing P/Al molar ratio of XPA supports, suggesting that phosphorus species in the form of phosphate group (PO_4) were transformed to tetrahedral phosphorus species such as $\text{P}(\text{OAl})_4$ [32]. As P/Al molar ratio increased, more phosphorus would be linked with oxygen atom connected to aluminum in the supports. In this way, the environments around aluminum and phosphorus species could be changed by varying P/Al molar ratio in the XPA supports.

3.2. Characterization of calcined Ni/XPA catalysts

Fig. 4(a) shows the nitrogen adsorption–desorption isotherms of calcined Ni/XPA ($X=0, 0.05$, and 0.20) catalysts. Although the isotherms of Ni/0.02PA and Ni/0.10PA catalysts were not shown here, it was observed that all the calcined Ni/XPA catalysts ($X=0, 0.02, 0.05, 0.10$, and 0.20) exhibited IV-type isotherms with H2-type hysteresis loops. This indicates that the calcined Ni/XPA catalysts still maintained a mesoporous structure like XPA supports

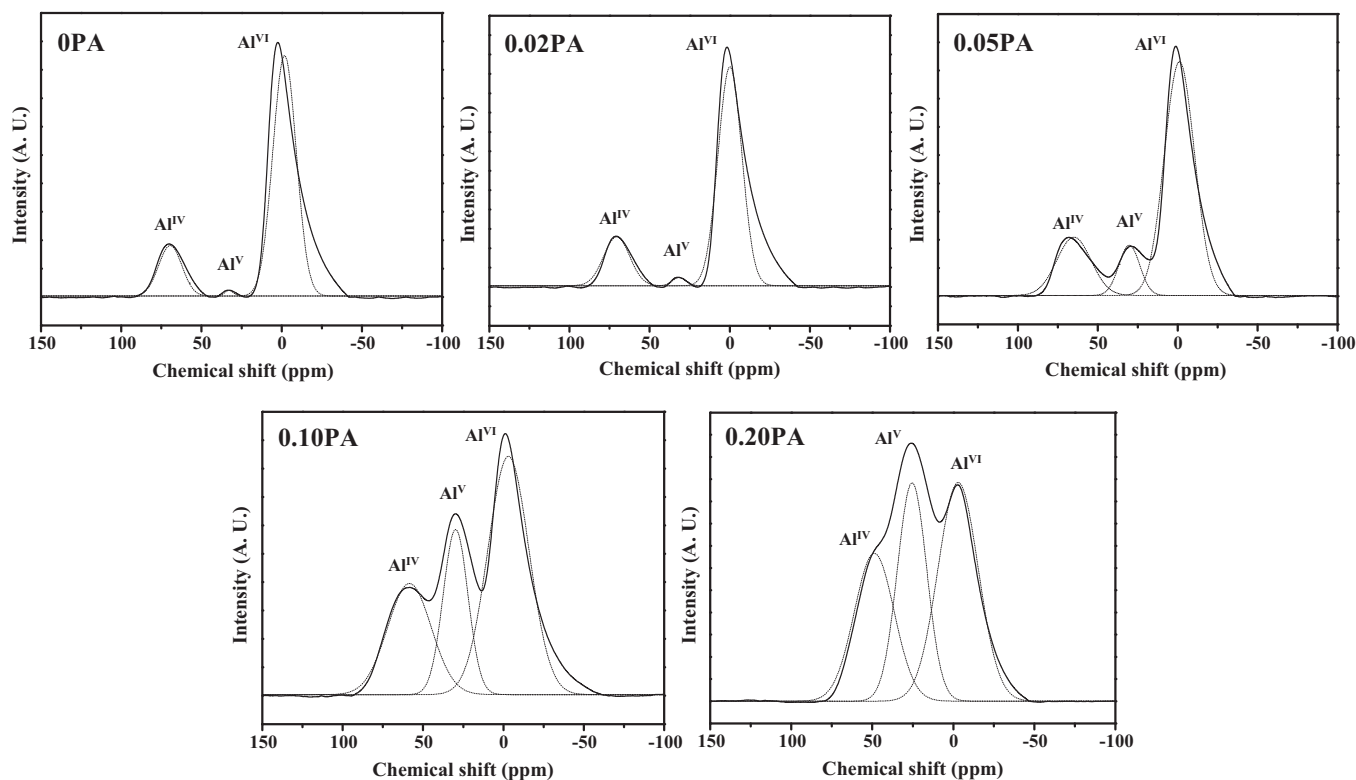


Fig. 2. ^{27}Al MAS NMR spectra of calcined XPA ($X = 0, 0.02, 0.05, 0.10$, and 0.20) supports.

Table 2

Chemical states of aluminum species in the XPA supports calcined at 700°C for 5 h.

Support	Chemical shift of penta-coordinated Al (ppm)	Relative distribution (%) ^a		
		Octa-coordinated Al (Al^{VI})	Penta-coordinated Al (Al^{V})	Tetra-coordinated Al (Al^{IV})
0PA	32.7	82.2	0.7	17.1
0.02PA	31.5	78.9	1.8	19.3
0.05PA	30.3	69.8	10.4	19.8
0.10PA	29.6	52.4	21.8	25.8
0.20PA	25.6	41.8	30.4	27.8

^a Calculated from the deconvoluted curve in Fig. 2.

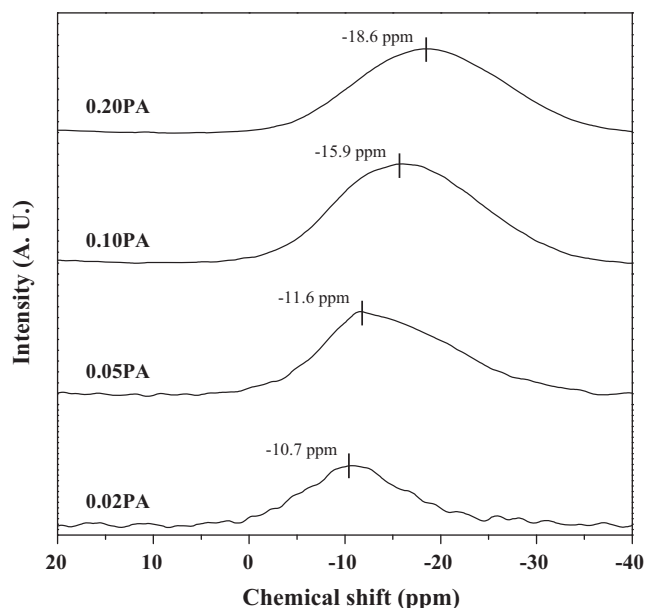


Fig. 3. ^{31}P MAS NMR spectra of calcined XPA ($X = 0.02, 0.05, 0.10$, and 0.20) supports.

(Fig. 1(a)). As summarized in Table 1, however, all the calcined Ni/XPA catalysts retained smaller surface area and smaller pore volume than the calcined XPA supports. This is because mesopores in the XPA supports were considerably blocked by nickel species during the impregnation step and deformed by the additional calcination step. On the other hand, Ni/XPA ($X = 0.02, 0.05, 0.10$, and 0.20) catalysts still retained larger surface area than Ni/OPA catalyst. This might be due to the fact that the calcined XPA support retained more penta-coordinated aluminum species which served as anchoring sites for nickel with increasing P/Al molar ratio, as discussed in Section 3.1.

Crystalline structures of calcined Ni/XPA ($X = 0, 0.02, 0.05, 0.10$, and 0.20) catalysts were investigated as presented in Fig. 4(b). Five diffraction peaks ascribed to nickel oxide phase (solid lines in Fig. 4(b)) were detected in all the calcined catalysts. Intensities of diffraction peaks for nickel oxide phase gradually increased with increasing P/Al molar ratio of calcined Ni/XPA catalysts. Although nickel aluminate phase (dashed lines in Fig. 4(b)) were also detected, intensities of nickel aluminate monotonically decreased with increasing P/Al molar ratio of calcined Ni/XPA catalysts. Thus, it can be inferred that nickel species existed in the form of nickel oxide and nickel aluminate, and the relative distribution of these forms was varied with P/Al molar ratio. In connection with NMR results of calcined XPA supports explained in Section 3.1, the

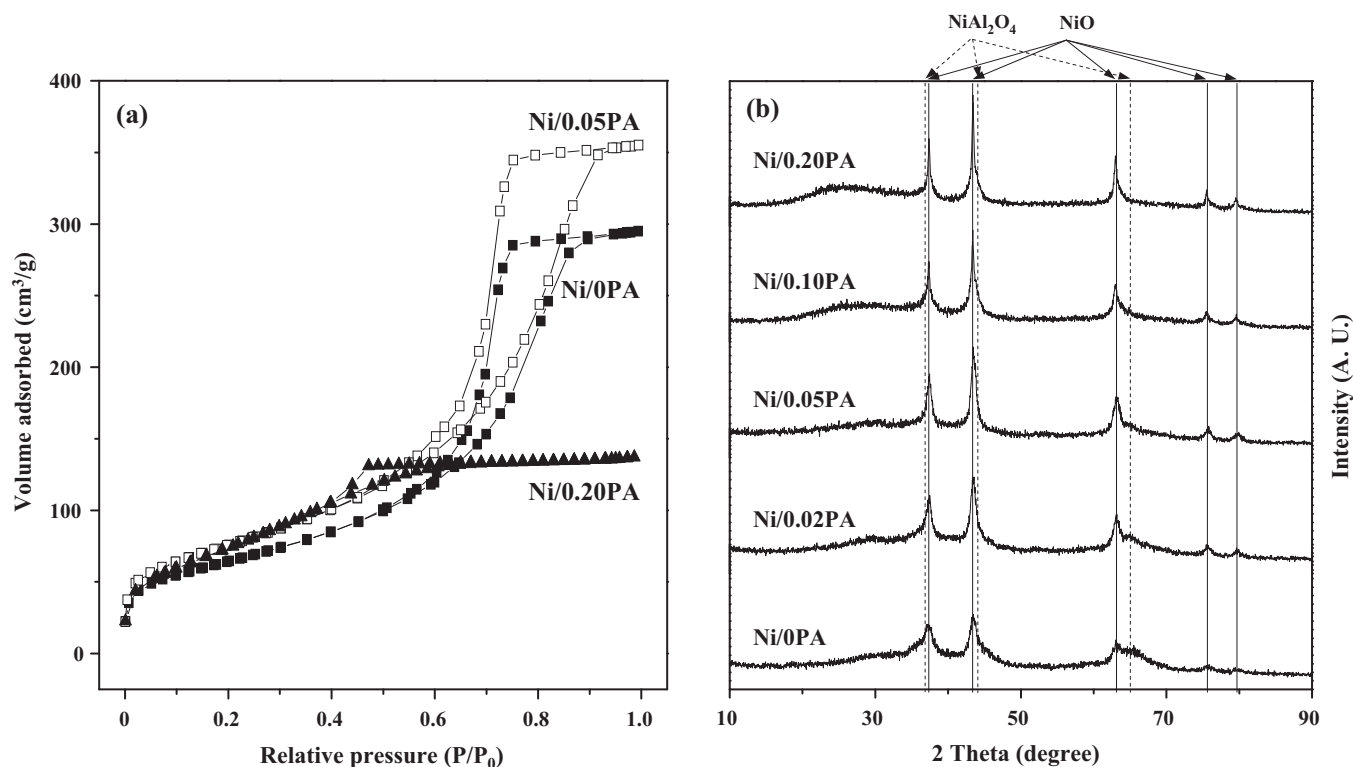


Fig. 4. (a) Nitrogen adsorption–desorption isotherms of calcined Ni/XPA ($X=0, 0.05$, and 0.20) catalysts, and (b) XRD patterns of calcined Ni/XPA ($X=0, 0.02, 0.05, 0.10$, and 0.20) catalysts.

XRD results revealed that nickel species dispersed in phosphorus-modified alumina support were gradually released from nickel aluminate spinel structure to nickel oxide phase on acidic aluminum species (coordinately unsaturated aluminum species) with increasing P/Al molar ratio. Therefore, the amount of aluminum species for anchoring nickel species increased while the strength of anchoring decreased with increasing P/Al molar ratio as discussed in ^{27}Al MAS NMR results. This resulted in the increase of nickel oxide phase which was known to have weaker metal-support interaction than nickel aluminate phase [34].

In order to examine metal-support interaction in the calcined Ni/XPA ($X=0, 0.02, 0.05, 0.10$, and 0.20) catalysts, TPR measurements were conducted as shown in Fig. 5(a). The reduction peaks detected at around $950\text{--}970^\circ\text{C}$ were associated with reduction of phosphorus species bound to oxygen [35]. It was observed that Ni/0.02PA catalyst did not show a reduction band within that temperature range. This might be because phosphorus content was too small to form a certain reducible phosphorus species. All the calcined Ni/XPA catalysts showed a reduction peak at around $733\text{--}757^\circ\text{C}$ which was attributed to reduction of nickel aluminate spinel or nickel oxide strongly interacted with alumina [36]. It is interesting to note that shape of this reduction peak was gradually changed more asymmetrically and the peak moved toward a higher temperature with increasing P/Al molar ratio of Ni/XPA ($X=0, 0.02, 0.05, 0.10$, and 0.20) catalysts. It is believed that the asymmetrical feature of the reduction band was due to the existence of nickel aluminate (NiAl_2O_4) and nickel oxide strongly interacted with support. The increased reduction peak temperature with increasing P/Al molar ratio of the catalysts was due to the enhanced metal-support interaction of nickel species in the form of nickel aluminate spinel, because phosphorus partly located in the XPA support induced lower degree of nickel saturation of the spinel [37]. Another peak attributed to reduction of bulk nickel oxide phase was detected

in the TPR profiles of Ni/0.10PA and Ni/0.20PA catalysts at around $349\text{--}374^\circ\text{C}$. Thus, it can be summarized that binding of nickel species in the form of nickel oxide in the phosphorus-modified alumina supports was weakened with increasing P/Al molar ratio, because affinity of acidic aluminum species toward nickel species decreased as discussed in ^{27}Al MAS NMR spectra of XPA supports. Although nickel species were still bound in the XPA support as a form of nickel aluminate or nickel oxide with strong metal-support interaction with increasing P/Al molar ratio until 0.05, some amounts of nickel species were excluded from the XPA support as a bulk nickel oxide phase when P/Al molar ratio was 0.1 and 0.2.

The above results were further confirmed by XPS analyses. Fig. 5(b) shows the XPS spectra in the Ni 2p level of calcined Ni/XPA ($X=0, 0.02, 0.05, 0.10$, and 0.20) catalysts. Deconvolution of the XPS spectra was performed by the Gaussian curve-fitting method. It has been reported that two Ni 2p_{3/2} peaks are observed at $855\text{--}856\text{ eV}$ and $853\text{--}854\text{ eV}$; the former is attributed to nickel species in the form of nickel aluminate or nickel oxide strongly interacted with support, while the latter is attributed to nickel species in the form of bulk nickel oxide [38]. However, one peak was detected in the XPS spectra of Ni/XPA ($X=0, 0.02$, and 0.05) catalysts due to the presence of nickel aluminate. On the other hand, Ni/0.10PA and Ni/0.20PA catalysts exhibited two peaks in the XPS spectra, representing that nickel species existed as nickel aluminate phase and bulk nickel oxide phase. Furthermore, binding energies of Ni 2p_{3/2} peak at $855\text{--}856\text{ eV}$ increased due to the increased metal-support interaction of nickel aluminate phase with increasing P/Al molar ratio until 0.20, as discussed in the TPR results. Additional XPS analyses for P 2p level of calcined catalysts (not shown here) revealed that phosphorus-related compounds such as nickel phosphate were not formed in the calcined Ni/XPA ($X=0.02, 0.05, 0.10$, and 0.20) catalysts.

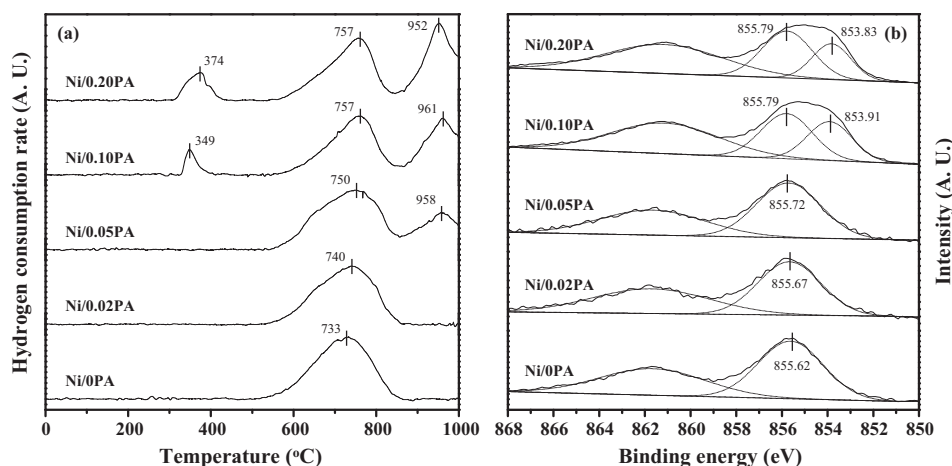


Fig. 5. (a) TPR profiles of calcined Ni/XPA ($X=0, 0.02, 0.05, 0.10$, and 0.20) catalysts, and (b) XPS spectra in the Ni 2p level of calcined Ni/XPA ($X=0, 0.02, 0.05, 0.10$, and 0.20) catalysts.

Fig. 6 represents the UV–vis–DRS spectra of calcined Ni/XPA ($X=0, 0.02, 0.05, 0.10$, and 0.20) catalysts. The reflectance band at 720 nm corresponds to nickel species with octahedral coordination (Ni_{oct}) normally formed in nickel oxide phase, while the bands at 600 and 640 nm are attributed to nickel species with tetrahedral coordination (Ni_{tet}) in nickel aluminate phase [39,40]. It was observed that the reflectance band of Ni_{oct} species (720 nm) became stronger with increasing P/Al molar ratio of Ni/XPA catalysts, demonstrating that $\text{Ni}_{\text{oct}}/\text{Ni}_{\text{tet}}$ ratio increased with increasing P/Al molar ratio. This indicates that the coordination of nickel species in the catalysts can be controlled by phosphorus addition. Ni_{oct} species are also known to be readily reducible compared to Ni_{tet} species. Thus, we can say that easily reducible nickel species were more formed with increasing P/Al molar ratio. This result was well consistent with TPR results showing that binding of nickel species in the form of nickel oxide in the supports was weakened due to the phosphorus addition.

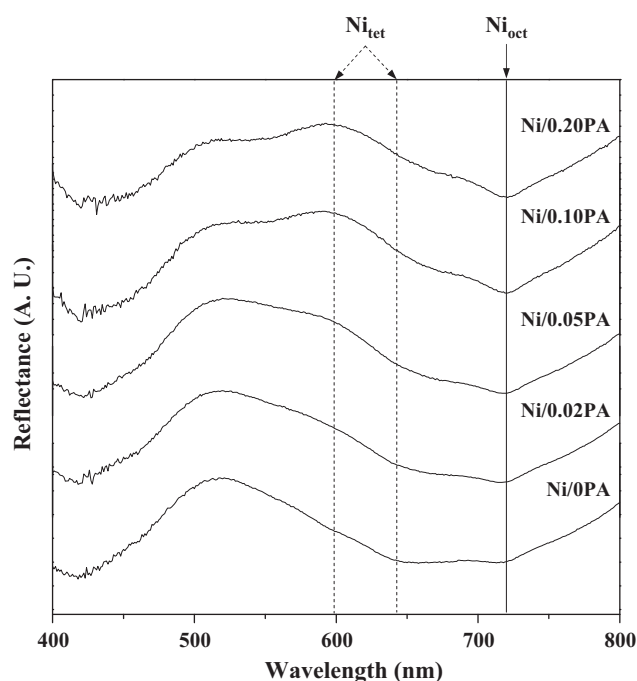


Fig. 6. UV–vis–DRS spectra of calcined Ni/XPA ($X=0, 0.02, 0.05, 0.10$, and 0.20) catalysts.

3.3. Characterization of reduced Ni/XPA catalysts

Crystalline phases of Ni/XPA ($X=0, 0.02, 0.05, 0.10$, and 0.20) catalysts reduced at 700 °C for 3 h were examined by XRD measurements. As shown in Fig. 7, all the reduced Ni/XPA catalysts retained metallic nickel phase (solid lines in Fig. 7). Diffraction peaks corresponding to nickel aluminate phase and nickel oxide phase were not detected in the XRD patterns. The diffraction peak of $\gamma\text{-Al}_2\text{O}_3$ (4 4 0) plane was also observed, indicating that the reduced Ni/XPA catalysts recovered original crystalline structure of calcined XPA supports by lattice contraction resulted from the release of nickel ions [22]. Thus, nickel species in the calcined Ni/XPA catalysts were completely reduced to metallic nickel phase during the reduction process employed in this work. Crystallite sizes of metallic nickel were also calculated as listed in Table 3. It was found that crystallite size of metallic nickel increased with increasing P/Al molar ratio in the reduced Ni/XPA catalysts. In particular, the reduced

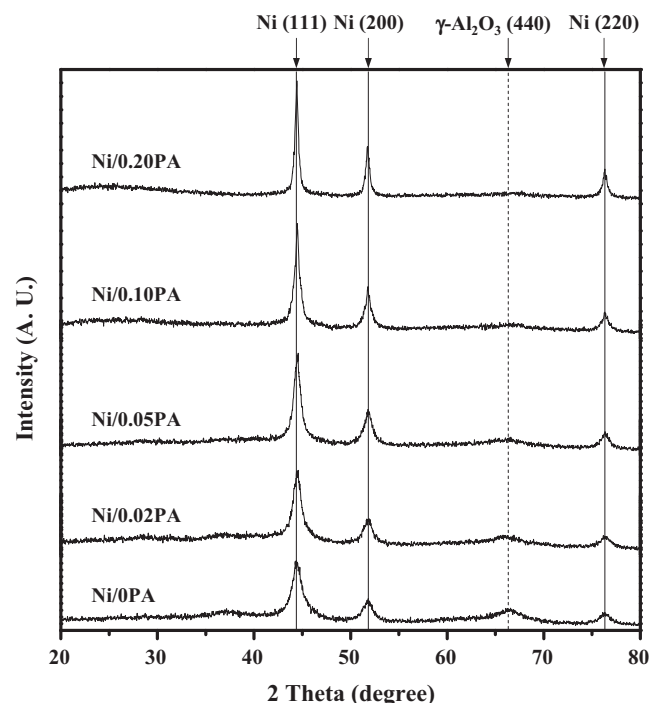


Fig. 7. XRD patterns of reduced Ni/XPA ($X=0, 0.02, 0.05, 0.10$, and 0.20) catalysts.

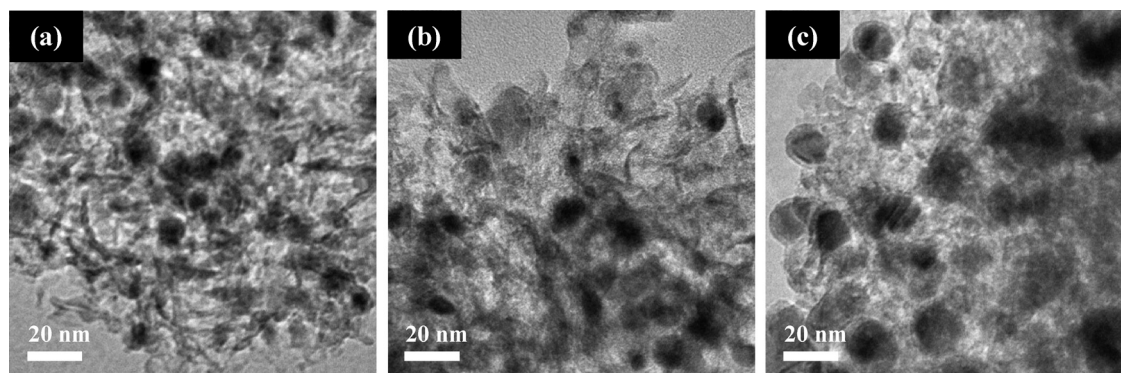


Fig. 8. TEM images of reduced (a) Ni/OPA, (b) Ni/0.05PA, and (c) Ni/0.20PA catalysts.

Ni/0.10PA and Ni/0.20PA catalysts showed a remarkable increment in the crystallite size of metallic nickel. It is generally accepted that nickel oxide phase rather than nickel aluminate phase is vulnerable to sintering at high temperature [34]. In consideration of XRD patterns of calcined Ni/XPA catalysts, therefore, it is believed that the increased amount of nickel oxide phase and the decreased amount of nickel aluminate phase with increasing P/Al molar ratio might be responsible for sintering of nickel species during the reduction process.

The trend of crystallite size of metallic nickel in the reduced Ni/XPA catalysts ($X=0, 0.05$, and 0.20) measured by XRD was also supported by TEM images. Fig. 8(a) shows well-dispersed nickel particles in the reduced Ni/OPA catalyst. The reduced Ni/0.05PA catalyst showed a similar size of nickel particles (Fig. 8(b)) compared to the reduced Ni/OPA catalyst. However, the reduced Ni/0.20PA catalyst (Fig. 8(c)) showed large nickel particles about 20 nm.

To make a detail comparison of nickel dispersion, H_2 -TPD measurements for reduced Ni/XPA ($X=0, 0.02, 0.05, 0.10$, and 0.20) catalysts were carried out as represented in Fig. 9. According to the literature [41], there are two hydrogen desorption regions; one (Type I) is attributed to hydrogen desorbed from the active metal species and the other (Type II) is related to hydrogen desorbed from subsurface layers or to spillover hydrogen. In order to distinguish these kinds of hydrogen in the H_2 -TPD profiles of the reduced Ni/XPA catalysts, H_2 -TPD profiles were deconvoluted into four bands with respect to desorption temperature; Type Ia ($<200^\circ\text{C}$), Type Ib ($200\text{--}400^\circ\text{C}$), Type Ic ($400\text{--}500^\circ\text{C}$), and Type II ($>500^\circ\text{C}$). The amount of hydrogen uptake by exposed nickel species of the catalysts was then calculated using deconvoluted peak area for Type I (Table 4). Total amount of hydrogen desorbed from the reduced Ni/XPA catalysts decreased with increasing P/Al molar ratio. This trend was in good agreement with the trend of crystallite size of metallic nickel. In addition, nickel surface area and nickel dispersion decreased with increasing P/Al molar ratio. This result implies the amount of exposed nickel species decreased with increasing P/Al molar ratio of reduced Ni/XPA catalysts.

It should be noted that there are some variations in distribution of hydrogen-binding sites over the catalysts. Especially, the amount

of strong hydrogen-binding sites showed a volcano-shaped trend with respect to P/Al molar ratio. Among the catalysts, Ni/0.05PA catalyst showed the largest amount of strong hydrogen-binding sites. This indicates that hydrogen molecules could be more strongly bound on the surface of nickel species in the reduced Ni/0.05PA catalyst compared to the other catalysts. In other words, nickel species in the reduced Ni/0.05PA catalyst was effective for stabilization of dissociated hydrogen atoms. It is believed that this is because nickel species in the reduced Ni/0.05PA catalyst are in the electronically favorable state for strong hydrogen-binding caused by high binding energy of nickel species in the XPA supports as evidenced in TPR and XPS results.

It has been reported that dissociative adsorption of methane on the surface of nickel species (Eq. (3)) is a rate-determining step in the steam reforming of methane [42]. For this reason, it is expected that stabilization of methyl group and hydrogen atom on nickel surface is important for efficient methane reforming on the nickel catalysts. Therefore, the reduced Ni/0.05PA catalyst was considered to be the most efficient for dissociative methane adsorption in

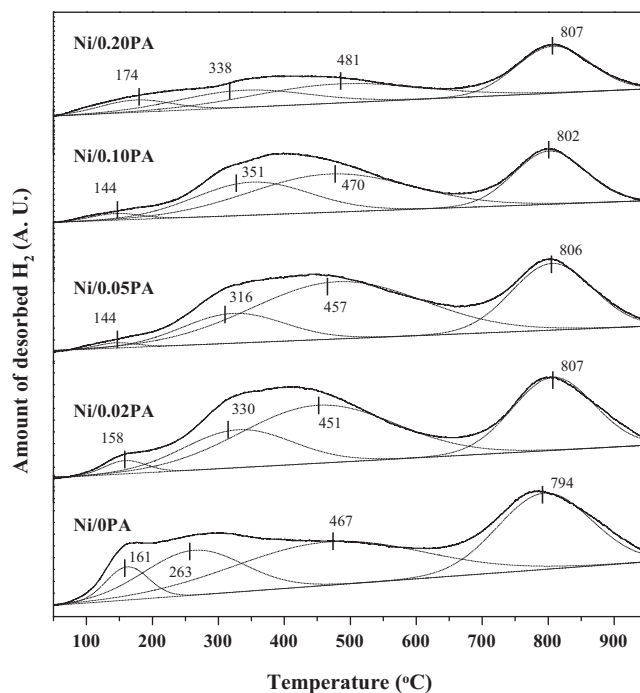


Fig. 9. H_2 -TPD profiles of reduced Ni/XPA ($X=0, 0.02, 0.05, 0.10$, and 0.20) catalysts.

Table 3
Crystallite sizes of metallic nickel in the Ni/XPA catalysts reduced at 700°C for 3 h.

Catalyst	Crystallite size of metallic nickel (nm) ^a
Ni/OPA	8.8
Ni/0.02PA	9.0
Ni/0.05PA	9.5
Ni/0.10PA	14.5
Ni/0.20PA	18.6

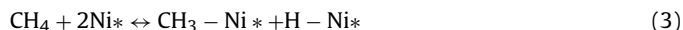
^a Calculated by the Scherrer equation from Ni (2 0 0) diffraction peak broadening in Fig. 7.

Table 4
H₂-TPD results of reduced Ni/XPA catalysts.

Catalyst	Amount of desorbed hydrogen (μmol-H ₂ /g) ^a				Nickel surface area (m ² /g-Ni) ^b	Nickel dispersion (%) ^c
	Weak site (Type Ia; <200 °C)	Medium site (Type Ib; 200–400 °C)	Strong site (Type Ic; 400–500 °C)	Total (Type Ia + Ib + Ic)		
Ni/OPA	9.4 (10.0%) ^c	29.8 (31.6%)	55.1 (58.4%)	94.3	44.2	6.6
Ni/0.02PA	3.7 (4.0%)	27.4 (30.1%)	60.1 (65.9%)	91.2	42.8	6.4
Ni/0.05PA	1.4 (1.6%)	20.3 (23.2%)	65.6 (75.2%)	87.3	40.9	6.2
Ni/0.10PA	1.8 (3.2%)	21.2 (36.8%)	34.5 (60.0%)	57.5	26.9	4.1
Ni/0.20PA	5.8 (13.8%)	14.7 (34.9%)	21.6 (51.3%)	42.1	19.7	3.0

^a Calculated from deconvoluted peak area of H₂-TPD profiles in Fig. 9.^b Calculated by assuming H/Ni_{atom} = 1.^c Values in parentheses are percentage of each deconvoluted area in H₂-TPD profiles.

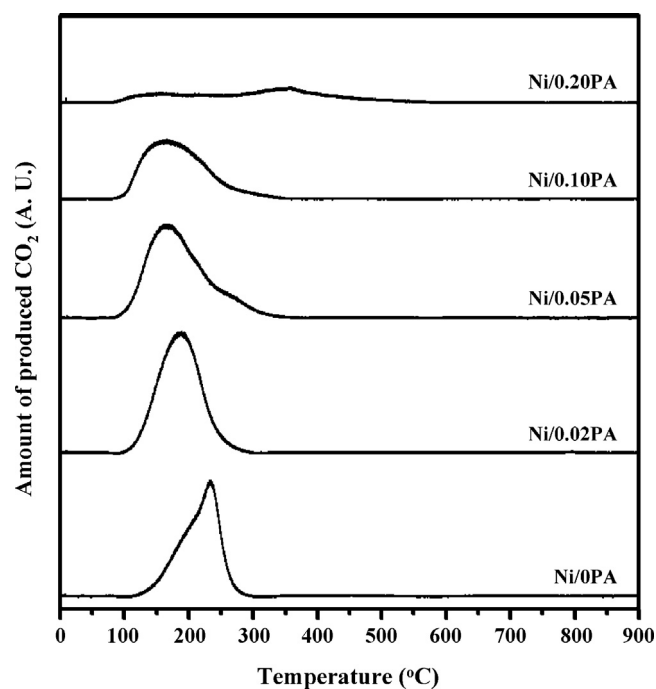
the steam reforming of LNG. This is further confirmed by CH₄-TPD measurements, as will be discussed in Section 3.4.



3.4. Methane adsorption study on reduced Ni/XPA catalysts

Methane (CH₄) is a major component of LNG which is a reactant in this study. Thus, CH₄-TPD measurements were carried out to explain the affinity of nickel species toward methane molecule and the trend of catalytic activities over Ni/XPA (X=0, 0.02, 0.05, 0.10, and 0.20) catalysts. It is important to note that desorption of methane on nickel–alumina catalyst can be regarded as temperature-programmed oxidation (TPO) of carbon species originated from methane, because residual surface oxygen species on the catalyst act as an oxidant [43]. In this study, therefore, adsorbed carbon species can be oxidized into carbon monoxide and carbon dioxide, or hydrogenated into methane due to hydrogen flow during the TPD measurements. However, a signal for carbon monoxide (*m/z* = 28) was not detected while signals for carbon dioxide (*m/z* = 44), methane (*m/z* = 15), and water (*m/z* = 18) were detected from ion chromatogram acquired using a GC–MSD. Water is generated by hydrogenation of oxygen species on the reduced Ni/XPA catalysts. Therefore, we used signals for carbon dioxide and methane to calculate the amount of adsorbed methane on the reduced Ni/XPA catalysts. CHNS elemental analyses were further carried out after CH₄-TPD measurements to examine residual carbon species on the catalysts. Indeed, it was revealed that the amount of carbon species hydrogenated into methane or remained on the catalysts was negligible, when compared to the amount of carbon species oxidized into carbon dioxide. Thus, we assumed that all the carbon species adsorbed on the surface of reduced Ni/XPA catalysts were oxidized into carbon dioxide. In other words, we assumed that the amount of carbon dioxide produced was identical to the amount of methane adsorbed on the surface of reduced Ni/XPA catalysts.

As presented in Fig. 10, a broad desorption band was observed in the CH₄-TPD profiles of reduced Ni/XPA (X=0, 0.02, 0.05, 0.10, and 0.20) catalysts. The amount of adsorbed methane on the catalysts was calculated as listed in Table 5. It was found that the amount of adsorbed methane increased in the order of Ni/0.20PA < Ni/0.10PA < Ni/OPA < Ni/0.02PA < Ni/0.05PA. This trend was well matched with the trend of the absolute amount of strong hydrogen-binding sites listed in Table 4, suggesting that methane

**Fig. 10.** CH₄-TPD profiles of reduced Ni/XPA (X=0, 0.02, 0.05, 0.10, and 0.20) catalysts.

adsorption behavior was closely related to the stabilization of chemisorbed hydrogen species. Fig. 11 shows the relationship between the amount of adsorbed methane and the absolute amount of strong hydrogen-binding sites. The amount of adsorbed methane increased with increasing the amount of strong hydrogen-binding

Table 5
Amount of adsorbed CH₄ on the reduced Ni/XPA catalysts.

Catalyst	Amount of adsorbed CH ₄ (μmol-CH ₄ /g) ^a
Ni/OPA	2.37
Ni/0.02PA	3.08
Ni/0.05PA	3.18
Ni/0.10PA	2.16
Ni/0.20PA	1.13

^a Calculated from peak area of CH₄-TPD profiles in Fig. 10.

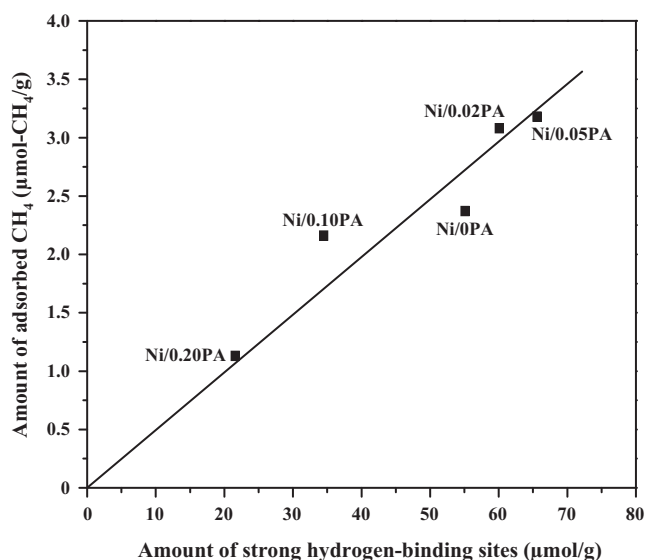


Fig. 11. (A) Correlation between the amount of adsorbed CH₄ in CH₄-TPD measurements and the amount of strong hydrogen-binding sites in H₂-TPD measurements of reduced Ni/XPA ($X=0, 0.02, 0.05, 0.10$, and 0.20) catalysts.

sites over the reduced Ni/XPA catalysts. Among the catalysts tested, Ni/0.05PA catalyst retaining the largest amount of strong hydrogen-binding sites exhibited the largest amount of adsorbed methane.

3.5. Catalytic performance in the hydrogen production by steam reforming of LNG over Ni/XPA catalysts

LNG conversion and hydrogen yield with time of stream in the hydrogen production by steam reforming of LNG over Ni/XPA ($X=0, 0.02, 0.05, 0.10$, and 0.20) catalysts are presented in Fig. 12. Ni/XPA ($X=0, 0.02$, and 0.05) catalysts exhibited a stable catalytic performance during the steam reforming of LNG. Well-developed mesoporosity of these catalysts was believed to be responsible for facilitating mass transfer of reactant molecules. In addition, small crystallite size of metallic nickel, high nickel surface area, and large amount of strong hydrogen-binding sites of these catalysts played crucial roles for their excellent catalytic performance. However, Ni/0.10PA and Ni/0.20PA catalysts experienced a catalyst deactivation. In particular, Ni/0.20PA catalyst showed a severe catalyst deactivation during the reaction; 25% decrease of LNG conversion and 65% decrease of hydrogen yield. The catalyst deactivation of Ni/0.10PA and Ni/0.20PA catalysts were mainly due to nickel sintering during the reaction. It was previously revealed that

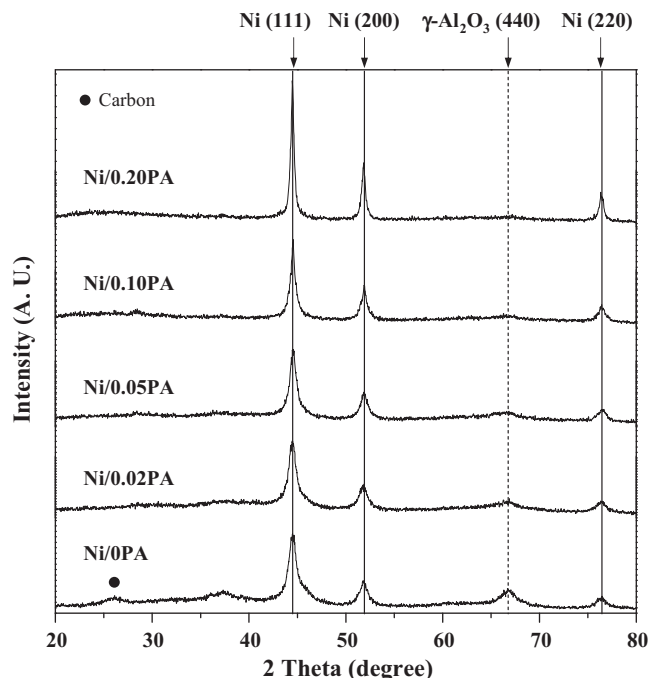


Fig. 13. XRD patterns of used Ni/XPA ($X=0, 0.02, 0.05, 0.10$, and 0.20) catalysts.

Ni/0.10PA and Ni/0.20PA catalysts retained relatively large crystallite size of metallic nickel caused by weak metal–support interaction between nickel species and support. Thus, nickel species weakly bound to the support in the Ni/0.10PA and Ni/0.20PA catalysts are vulnerable to sintering during the reaction. Nickel sintering was quantitatively examined by XRD measurements for the used catalysts after a 1000 min-reaction (Fig. 13). The calculated crystallite size of metallic nickel in the used catalysts is listed in Table 6. Crystallite size of metallic nickel on the used Ni/XPA ($X=0, 0.02, 0.05, 0.10$, and 0.20) catalysts was larger than that on the reduced catalysts (Table 3). In addition, the degree of sintering of Ni/0.10PA and Ni/0.20PA catalysts was much higher than that of the other Ni/XPA catalysts. The amount of carbon deposition in the used catalysts is listed in Table 7. It is noticeable that the amount of carbon deposition decreased with increasing P/Al molar ratio of the catalysts. This might be due to the basic nature of phosphorus species which served as an electron donor as reported in the literature [44]. From these results, it is believed that nickel sintering rather than carbon deposition was a main factor

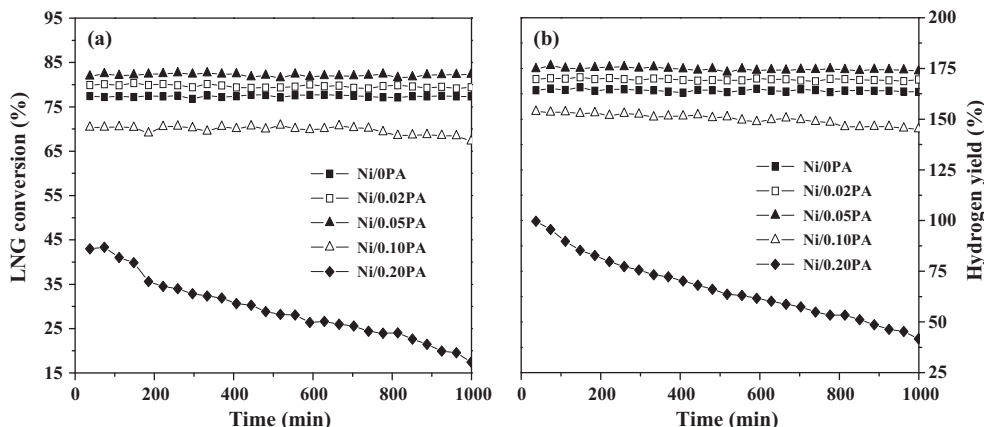


Fig. 12. (a) LNG conversion and (b) hydrogen yield with time on stream in the steam reforming of LNG over Ni/XPA ($X=0, 0.02, 0.05, 0.10$, and 0.20) catalysts at 600 °C.

Table 6

Crystallite sizes of metallic nickel and degree of sintering of the used Ni/XPA catalysts after a 1000 min-reaction.

Catalyst	Crystallite size of metallic nickel (nm) ^a	Degree of sintering (%) ^b
Ni/OPA	9.0	2.6
Ni/0.02PA	9.2	3.0
Ni/0.05PA	10.0	4.9
Ni/0.10PA	16.4	12.9
Ni/0.20PA	22.2	19.3

^a Calculated by the Scherrer equation from Ni (2 0 0) diffraction peak broadening in Fig. 13.

^b Calculated by following equation: Degree of sintering(%) = $\frac{\text{Crystallite size of metallic nickel after reaction (nm)}}{\text{Crystallite size of metallic nickel after reduction (nm)}} \times 100$

Table 7

Amount of carbon deposition in the used Ni/XPA catalysts after a 1000 min-reaction.

Catalyst	Amount of carbon deposition (wt%) ^a
Ni/OPA	7.8
Ni/0.02PA	0.5
Ni/0.05PA	0.2
Ni/0.10PA	0.1
Ni/0.20PA	–

^a Determined by CHNS elemental analysis.

for catalyst deactivation of Ni/0.10PA and Ni/0.20PA catalysts during the steam reforming reaction.

Fig. 14 shows the initial LNG conversion and initial hydrogen yield over Ni/XPA (X=0, 0.02, 0.05, 0.10, and 0.20) catalysts in the steam reforming of LNG plotted as a function of P/Al molar ratio. Initial LNG conversion and initial hydrogen yield exhibited volcano-shaped curves with respect to the P/Al molar ratio. It was found that both initial LNG conversion and initial hydrogen yield decreased in the order of Ni/0.05PA > Ni/0.02PA > Ni/OPA > Ni/0.10PA > Ni/0.20PA. This indicates that an optimal P/Al molar ratio was required for maximum hydrogen production by steam reforming of LNG over Ni/XPA catalysts. These catalytic performance data were also well correlated with the amount of adsorbed methane which was related to the affinity toward methane of Ni/XPA catalysts, as presented in Fig. 15. As the amount of adsorbed methane increased, LNG conversion and hydrogen yield over Ni/XPA catalysts increased. In other words, catalytic performance of Ni/XPA catalysts was enhanced with increasing the amount of active sites available for methane

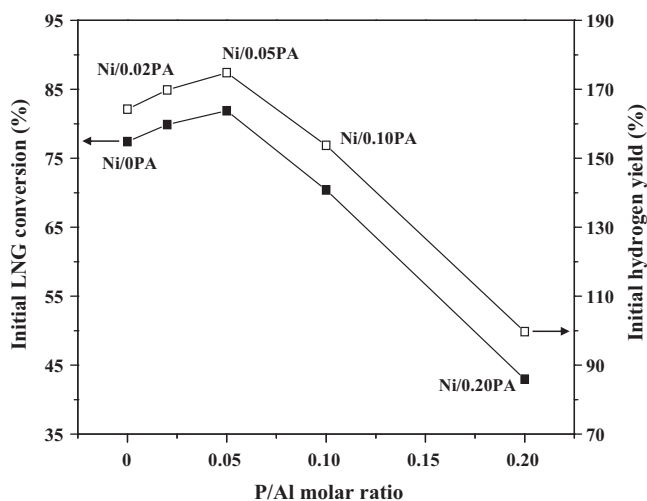


Fig. 14. Correlations between initial catalytic performance and P/Al molar ratio of Ni/XPA (X=0, 0.02, 0.05, 0.10, and 0.20) catalysts.

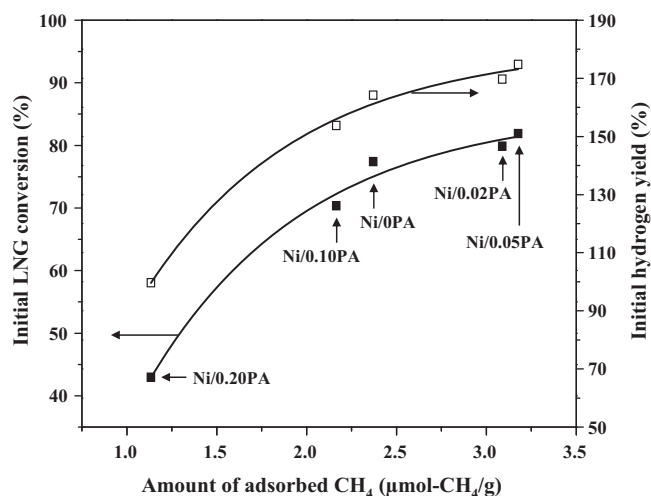


Fig. 15. Correlations between initial catalytic performance and the amount of adsorbed CH₄ calculated in the CH₄-TPD profiles of Ni/XPA (X=0, 0.02, 0.05, 0.10, and 0.20) catalysts.

adsorption. Among the catalysts tested, Ni/0.05PA catalyst with the highest affinity toward methane served as the most efficient catalyst in the hydrogen production by steam reforming of LNG.

4. Conclusions

A series of nickel catalysts supported on mesoporous phosphorus-modified alumina xerogel (Ni/XPA, X=0, 0.02, 0.05, 0.10, and 0.20) were prepared by an epoxide-driven sol–gel method and a subsequent incipient impregnation method, and they were employed to the hydrogen production by steam reforming of simulated LNG. The effect of P/Al molar ratio on the physicochemical properties and catalytic activities of Ni/XPA catalysts in the steam reforming of LNG was investigated. All the calcined phosphorus-modified alumina supports (XPA) showed a mesoporous structure. In particular, XPA supports retained much amount of penta-coordinated aluminum species and P(OAl)₄ units with increasing P/Al molar ratio. All the calcined Ni/XPA catalysts still retained a mesoporous structure even after the nickel impregnation, and they showed co-existence of nickel oxide phase and nickel aluminate phase. In the TPR and XPS analyses, it was found that the addition of phosphorus affected the metal-support interaction and binding energies of nickel species in the calcined Ni/XPA catalysts. Especially, Ni/0.05PA catalyst showed the highest binding energy for nickel species. Crystallite size of metallic nickel increased with increasing P/Al molar ratio of the reduced Ni/XPA catalysts. H₂-TPD measurements revealed that the amount of strong hydrogen-binding sites of the reduced Ni/XPA catalysts showed a volcano-shaped trend. Furthermore, the amount of adsorbed methane measured by CH₄-TPD measurements was well correlated with the amount of strong hydrogen-binding sites of the catalysts. In the steam reforming of LNG, Ni/XPA (X=0, 0.02, and 0.05) catalysts showed a stable catalytic performances while Ni/0.10PA and Ni/0.20PA catalysts experienced a catalyst deactivation due to nickel sintering. Although carbon deposition was suppressed by phosphorus addition in the Ni/XPA catalysts, nickel sintering rather than carbon deposition was much related to the catalyst deactivation. Initial catalytic performance of Ni/XPA (X=0, 0.02, 0.05, 0.10, and 0.20) catalysts in the steam reforming of LNG showed volcano-shaped curves with respect to the P/Al molar ratio. Thus, an optimal P/Al molar ratio was required for efficient hydrogen production by steam reforming of LNG over Ni/XPA catalyst. LNG conversion and hydrogen yield were also closely related to the amount of adsorbed

methane on the catalysts. The catalytic performance of Ni/XPA catalysts increased with increasing the amount of adsorbed methane on the catalysts.

Acknowledgments

This work was supported by the Global Frontier R&D Program on Center for Multiscale Energy System funded by the National Research Foundation under the Ministry of Science, ICT & Future Planning, Korea (2012M3A6A7054866).

References

- [1] S. Dunn, Int. J. Hydrogen energy 27 (2002) 235–264.
- [2] M. Poliakoff, P. Licence, Nature 450 (2007) 810–812.
- [3] C.A. Franchini, W. Aranzuez, A.M.D. Farias, G. Pecchi, M.A. Fraga, Appl. Catal., B 147 (2014) 193–202.
- [4] I. Dincer, Int. J. Hydrogen Energy 37 (2012) 1954–1971.
- [5] A. Haryanto, S. Fernando, N. Murali, S. Adhikari, Energy Fuels 19 (2005) 2098–2106.
- [6] S. Ahmed, M. Krumpelt, Int. J. Hydrogen Energy 26 (2001) 291–301.
- [7] U. Eberle, B. Muller, R. von Helmolt, Energy Environ. Sci. 5 (2012) 8780–8798.
- [8] J.N. Armor, Appl. Catal., A 176 (1999) 159–176.
- [9] Y. Bang, S.J. Han, J. Yoo, J.H. Choi, K.H. Kang, J.H. Song, J.G. Seo, J.C. Jung, I.K. Song, Int. J. Hydrogen Energy 38 (2013) 8751–8758.
- [10] J.G. Seo, M.H. Youn, I.K. Song, Catal. Surv. Asia 14 (2010) 1–10.
- [11] Y. Bang, S.J. Han, J.G. Seo, M.H. Youn, J.H. Song, I.K. Song, Int. J. Hydrogen Energy 37 (2012) 17967–17977.
- [12] S. Wang, G.Q.M. Ju, Appl. Catal., B 16 (1998) 269–277.
- [13] H.S. Bengaard, J.K. Nørskov, J. Sehested, B.S. Clausen, L.P. Nielsen, A.M. Molenbroek, J.R. Rostrup-Nielsen, J. Catal. 209 (2002) 365–384.
- [14] J.R. Rostrup-Nielsen, Catal. Today 63 (2000) 159–164.
- [15] H. Jeong, M. Kang, Appl. Catal., B 95 (2010) 446–455.
- [16] J.G. Seo, M.H. Youn, K.M. Cho, S. Park, I.K. Song, J. Power Sources 173 (2007) 943–949.
- [17] J. Xu, C.M.Y. Yeung, J. Ni, F. Meunier, N. Acerbi, M. Fowles, S.C. Tsang, Appl. Catal., A 345 (2008) 119–127.
- [18] O. Yamazaki, K. Tomishige, K. Fujimoto, Appl. Catal., A 136 (1996) 49–56.
- [19] F. Bimbela, D. Chen, J. Ruiz, L. García, J. Arauzo, Appl. Catal., B 119–120 (2012) 1–12.
- [20] J. Xu, L. Chen, K.F. Tan, A. Borgna, M. Saeys, J. Catal. 261 (2009) 158–165.
- [21] D.L. Hoang, S.H. Chan, O.L. Ding, J. Power Sources 159 (2006) 1248–1257.
- [22] L. Pelletier, D.D.S. Liu, Appl. Catal., A 317 (2007) 293–298.
- [23] S. Chen, Y. Zhang, M. Wu, W. Fang, Y. Yang, Appl. Catal., A 431–432 (2012) 151–156.
- [24] T.F. Baumann, A.E. Gash, S.C. Chinn, A.M. Sawvel, R.S. Maxwell, J.H. Satcher Jr., Chem. Mater. 17 (2005) 395–401.
- [25] A.E. Gash, T.M. Tillotson, J.H. Satcher Jr., J.F. Poco, L.W. Hrubesh, R.L. Simpson, Chem. Mater. 13 (2001) 999–1007.
- [26] T.-Y. Wei, C.-H. Chen, H.-C. Chien, S.-Y. Lu, C.-C. Hu, Adv. Mater. 22 (2010) 347–351.
- [27] K.S.W. Sing, D.H. Everett, R.A.W. Haul, L. Moscou, R.A. Pierotti, J. Rouquerol, T. Siemieniowska, Pure Appl. Chem. 57 (1985) 603–619.
- [28] W. Cai, J. Yu, C. Anand, A. Vinu, M. Jaroniec, Chem. Mater. 23 (2011) 1147–1157.
- [29] T. Onfroy, W.-C. Li, F. Schüth, H. Knözinger, Phys. Chem. Chem. Phys. 11 (2009) 3671–3679.
- [30] Y. Kim, C. Kim, P. Kim, J. Yi, J. Non-Cryst. Solids 351 (2005) 550–556.
- [31] X. Krokidis, P. Raybaud, A.-E. Gobichon, B. Rebours, P. Euzen, H. Toulhoat, J. Phys. Chem. B 105 (2001) 5121–5130.
- [32] J.S. Valente, S. Falcón, E. Lima, M.A. Vera, P. Bosch, E. López-Salinas, Microporous Mesoporous Mater. 94 (2006) 277–282.
- [33] J.H. Kwak, J.Z. Hu, D.H. Kim, J. Szanyi, C.H.F. Peden, J. Catal. 251 (2007) 189–194.
- [34] P. Salagre, J.L.G. Fierro, F. Medina, J.E. Sueiras, J. Mol. Catal. A: Chem. 106 (1996) 125–134.
- [35] J. Chen, L. Sun, R. Wang, J. Zhang, Catal. Lett. 133 (2009) 346–353.
- [36] A.N. Kharat, P. Pendleton, A. Badalyan, M. Abedini, M.M. Amini, J. Catal. 205 (2002) 7–15.
- [37] R. Yang, X. Li, J. Wu, X. Zhang, Z. Zhang, Y. Cheng, Appl. Catal., A 368 (2009) 105–112.
- [38] S. Natesakhawat, R.B. Watson, X. Wang, U.S. Ozkan, J. Catal. 234 (2005) 496–508.
- [39] R. López-Fonseca, C. Jiménez-González, B. Rivas, J.I. Gutiérrez-Ortiz, Appl. Catal., A 437–438 (2012) 53–62.
- [40] S. Damyanova, B. Pawelec, K. Arishtirova, J.L.G. Fierro, Int. J. Hydrogen Energy 36 (2011) 10635–10647.
- [41] S. Velu, S.K. Gangwal, Solid State Ionics 177 (2006) 803–811.
- [42] D.L. Trimm, Stud. Surf. Sci. Catal. 36 (1987) 39–50.
- [43] L. Qian, Z. Yan, J. Nat. Gas Chem. 11 (2002) 151–158.
- [44] S.E. Denmark, G.L. Beutner, Angew. Chem. Int. Ed. 47 (2008) 1560–1638.